

CHEMICAL PHYSICS

Optical suppression of energy barriers in single molecule-metal binding

Qianqi Lin^{1†}, Shu Hu^{1†}, Tamás Földes^{2,3}, Junyang Huang¹, Demelza Wright¹, Jack Griffiths¹, Eoin Elliott¹, Bart de Nijs¹, Edina Rosta^{2,3}, Jeremy J. Baumberg^{1*}

Transient bonds between molecules and metal surfaces underpin catalysis, bio/molecular sensing, molecular electronics, and electrochemistry. Techniques aiming to characterize these bonds often yield conflicting conclusions, while single-molecule probes are scarce. A promising prospect confines light inside metal nanogaps to elicit in operando vibrational signatures through surface-enhanced Raman scattering. Here, we show through analysis of more than a million spectra that light irradiation of only a few microwatts on molecules at gold facets is sufficient to overcome the metallic bonds between individual gold atoms and pull them out to form coordination complexes. Depending on the molecule, these light-extracted adatoms persist for minutes under ambient conditions. Tracking their power-dependent formation and decay suggests that tightly trapped light transiently reduces energy barriers at the metal surface. This opens intriguing prospects for photocatalysis and controllable low-energy quantum devices such as single-atom optical switches.

INTRODUCTION

Understanding the interactions between molecules and metal surfaces is of widespread importance in both fundamental science and evolving technologies, with prominent examples spanning electrochemistry (1), catalysis (2), organic solar cells (3), biosensing (4), and medical imaging/targeting (5). In particular, there has been tremendous interest in using molecule-metal transient bonds for the development of molecular electronics (6–8) and spintronics (9–11) to enable ultrahigh-density information devices for low-energy and compact upscaled data storage.

To study molecule-metal surface interactions, spectroscopic techniques such as Raman or infrared absorption have great utility since they work in ambient conditions, are nondestructive, and can track dynamics, resolve transient species, and work in electrochemical environments (12). To avoid problematic averaging over many different sites and conformations, the confinement of optical fields to atomic scales has enabled vibrational spectroscopy of single molecules at the metal interface. Plasmonic field localization to picometer length scales on metals (termed picocavities) depends on individual metal adatoms, as described by recent theories (13–15). Tip-enhanced (16–18) and surface-enhanced (19–22) Raman spectroscopies (TERS and SERS) now reach this picocavity regime.

Extensive experiments and modeling of adatoms using scanning tunneling microscopy (often in ultrahigh vacuum at cryogenic temperatures) have shown typical $U_f^0 \sim 1$ eV adatom formation energies (for coinage metals), as well as ~ 1 eV surface diffusion barriers (23–27), both key energy scales in catalysis. However, how these change with molecule-metal interactions or with light and how they link to picocavity formation in metal nanogaps are not understood (28). This is exacerbated by the challenge of unifying quantum molecular modeling with classical electromagnetism on these atomic length scales (29).

In this work, we demonstrate how the molecule-metal opto-chemical interaction directly influences the formation and stabilization of light-induced adatoms yielding picocavities. Previously, we showed how picocavities give vibrational spectra from single molecules (19, 21) but were unable to shed light on the mechanisms for how they are formed. Here, we show that power-dependent creation rates depend crucially on the molecular species in their vicinity, a key constraint to any proposed mechanism. We emphasize that while the temperature of the metal remains near room temperature (evidenced directly in the SERS), optical heating would instead require $T > U_f^0/k_B \sim 12,000$ K to overcome the adatom formation barrier $U_f^0 \sim 1$ eV and extract a single Au⁽⁰⁾ atom from the gold surface. After presenting the data, we discuss what models might account for the observations. Our results suggest the mechanism to be opto-molecular tuning of the energy barrier at metal surfaces, which opens up opportunities for controlling reactions at the single-atom and single-molecule level, with promise in catalysis, optical switching, quantum devices, and molecular optoelectronics.

RESULTS

Plasmonic nanocavity assembly

To confine the light sufficiently tightly, we construct nanocavities from nanoparticle-on-mirror (NPoM) plasmonic gaps (Fig. 1A) that can incorporate a wide range of molecules. A self-assembled monolayer (SAM) is immobilized onto planar gold ‘mirror’ substrates with gold nanoparticles (AuNPs) and then drop-cast on top. We focus on monolayers of biphenyl-4-thiol (BPT; purple in Fig. 1), 4-mercaptobenzonitrile (MBN; brown), and 4-mercaptopyridine (MPy; cyan) sandwiched inside the gaps but emphasize that most molecules give similar results (others in fig. S1) (21, 30). The dipolar coupling between the nanoparticle and its image charges in the mirror creates a strong electromagnetic field tightly confined in the nanoscale hotspot between the facets (Fig. 1A, inset), enhancing Raman scattering by $>10^9$. The properties of the monolayer can be characterized by dark-field scattering spectra of the NPoMs giving their nanocavity resonant wavelengths (λ_c) (fig. S2) (31). Irradiating NPoMs with a laser at 633 nm gives efficiently outcoupled SERS spectra suited for

Copyright © 2022
The Authors, some
rights reserved;
exclusive licensee
American Association
for the Advancement
of Science. No claim to
original U.S. Government
Works. Distributed
under a Creative
Commons Attribution
License 4.0 (CC BY).

Downloaded from https://www.science.org at Cambridge University on June 27, 2022

¹Nanophotonics Centre, Department of Physics, Cavendish Laboratory, University of Cambridge, Cambridge CB3 0HE, England, UK. ²Department of Chemistry, King's College London, 7 Trinity Street, London SE1 1DB, UK. ³Department of Physics and Astronomy, University College London, London WC1E 6BT, UK.

*Corresponding author. Email: jjb12@cam.ac.uk
†These authors contributed equally to this work.

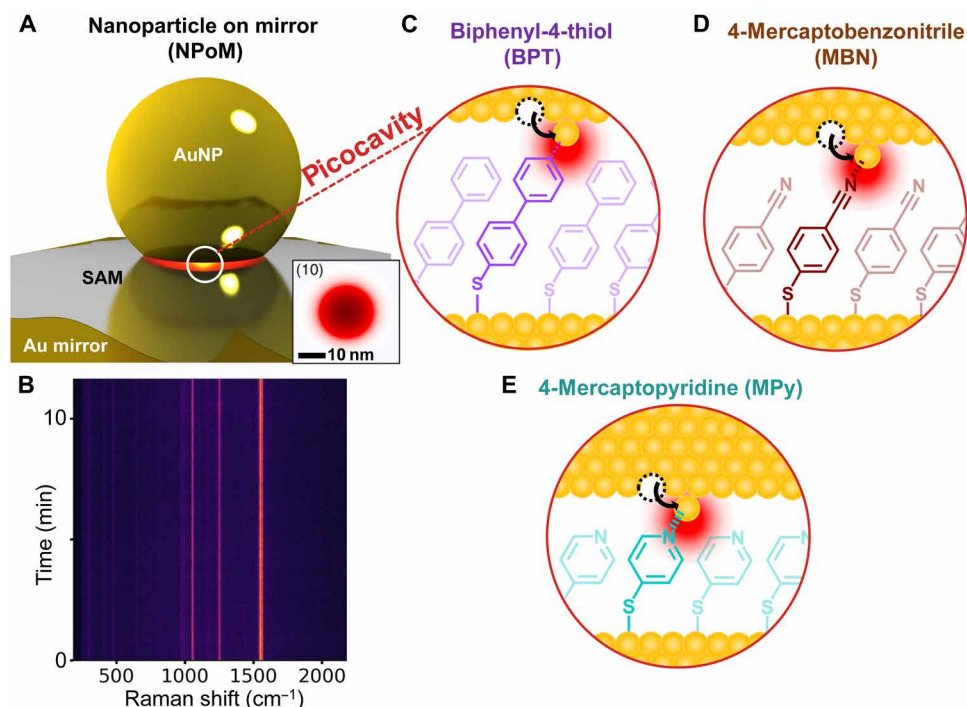


Fig. 1. Light-activated molecular control of adatoms. (A) NPoM geometry, sandwiching a SAM of either BPT (purple), MBN (brown), or MPy (cyan). Optical field at plasmon resonance is trapped in the nanogap (inset shows cross section under facet through the gap center). (B) SERS spectra from BPT NPoM every 100 ms at 20 μ W, showing no picocavities at low power. (C to E) Picocavities formed by a single adatom protrusion.

rapid spectral acquisition at subsecond rates with powers down to 1 μ W, without substantially heating them (see Materials and Methods). At low powers, no picocavities are observed (Fig. 1B).

Adatom movement

In SERS time series (Figs. 2, A to C, and 1B), persistent lines with constant intensity originate from the few hundred molecules located within the nanocavity hotspot (black spectra in Fig. 2, D to F) (28). Their identity is confirmed by comparison with density functional theory (DFT) calculations (Fig. 2, G to I; see Materials and Methods). Upon strong enough illumination, two types of atomic surface reconstructions are seen to occur at the surrounding metal facets. In the first type, picocavities (19, 21, 22) arise from single Au⁽⁰⁾ atoms pulled out of the gold surface (Fig. 1, C to E). Threefold larger field enhancements at the protruding adatom (compared to the nanocavity) give strong enough SERS ($\propto 3^4 \sim 80$) to see a single molecule nearby (red, Fig. 2, D to F) above that of all other hotspot molecules together. Picocavity spectra show intense new vibrational modes that vary in both intensity and frequency through fluctuations in the single adatom-molecule coordination bond that is shown to form (21), as seen in DFT simulations (fig. S3) (21) [the vibrational energy fluctuations evidence single molecules, vibrations downshift as coordination bonds capture electron density (32), and selection rules break in the high field gradients]. While, very occasionally, two molecules appear with correlated vibrational fluctuations, almost always, only a single picocavity molecule is observed, hence the conclusion that only single Au adatoms are involved for each. Experiments using different laser wavelengths show that these picocavities are predominantly located away from the facet edges

(33), near the facet center where the optical fields are strongest (Fig. 1A, inset).

In the second type, ‘flares’ (30) arise from a region of the facet behaving differently from the bulk material. Their origin has been suggested as enhanced optical field penetration into the metal in these patches, increasing the electronic Raman scattering (ERS) (30); however, alternative explanations remain possible (34). These intense flares have broad spectra (blue, Fig. 2, D to F) that are different each time, but independent of molecule species. The lifetimes of picocavities and flares ($T_{p,f}$ respectively; Fig. 2A) can be measured once formed, while statistics of their formation times ($\tau_{p,f}$) after the start of irradiation (or their average number per unit time) give their excitation rates (Fig. 3).

Effect of light, molecule type, and temperature Formation rates

To understand the opto-molecular-induced effects on picocavities and flares, thousands of time series of SERS spectra are recorded by running automated measurements using NPoM tracking software (35), with power-series laser irradiation from 2 to 200 μ W on many different NPoMs across each sample (Fig. 3). This enables conclusions to be drawn without depending on the specific nanoparticle (near-spherical) shape and facet. Within a time series, the spectral dissimilarity metric of their Euclidean distance (36) and a supervised machine learning model (fig. S5) are used to discern picocavities and flares. This analysis generates statistics (table S1 to S4) that identify formation and decay rates. Exponential probability distributions are seen in all cases (Fig. 3, A and B), suggesting that a single formation process is likely responsible (notes S3 and S4).

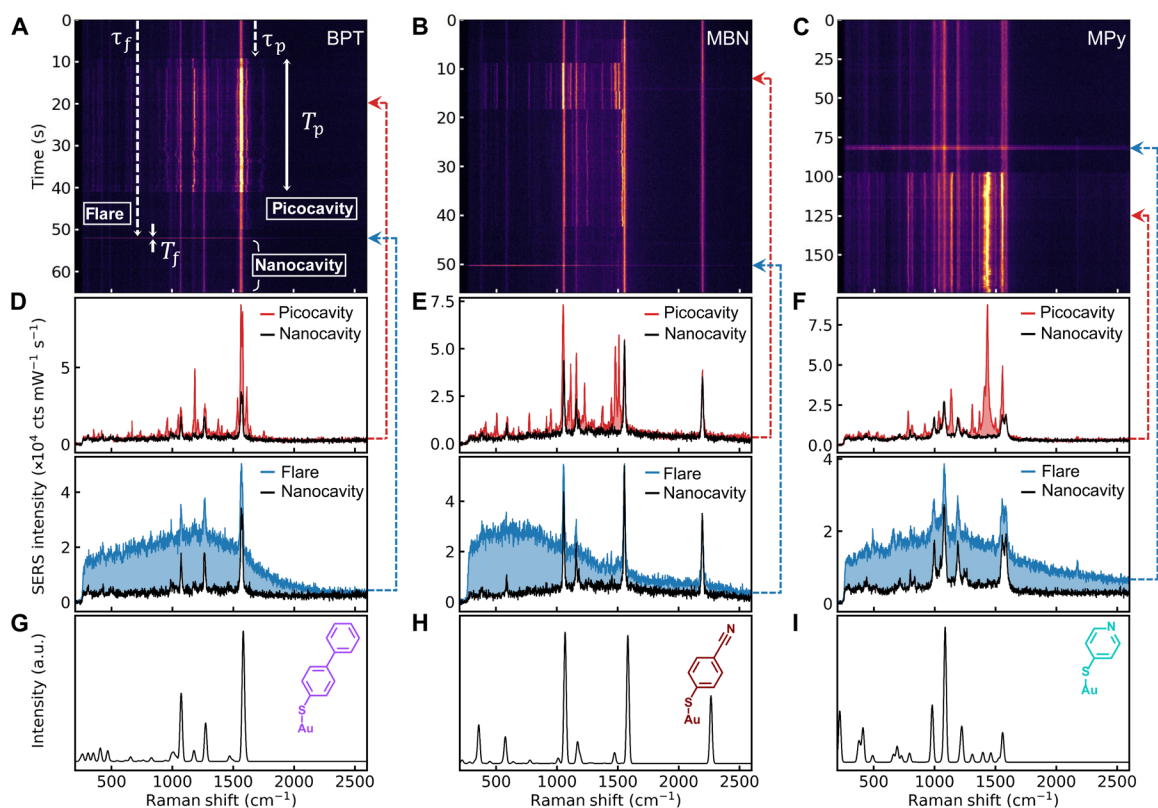


Fig. 2. Raman time evolution of picocavities and flares. (A) Time-series SERS spectra of BPT for 50- μ W 633-nm laser irradiation. Examples of a nanocavity, a picocavity, and a flare are shown: τ_p is the formation time before a picocavity is observed, T_p is the lifetime of a picocavity, and τ_f and T_f are the formation time and lifetime of a flare. (B) Time-series SERS spectra of MBN for 50- μ W irradiation. (C) Time-series SERS spectra of MPy for 10- μ W irradiation. (D to F) Example SERS spectra from the nanocavity (black, $t = 0$ s), a picocavity (red), and a flare (blue). (G to I) DFT-calculated Raman spectra with the corresponding molecular structures in the insets. a.u., arbitrary units.

The formation rate of picocavities (P_p ; Fig. 3C) initially rises slowly with laser intensity (I), increasing rapidly above an intensity threshold, before saturating at P_{op} . This is seen across all molecules measured [at $T = 300$ K, and for BPT, at 10 K (19); tables S1 and S3]. The critical intensity threshold I_c taken as $P_p(I_c) = e^{-1}P_{op}$ is found at $I_c = 97, 51,$ and $5.5 \mu\text{W } \mu\text{m}^{-2}$ for BPT, MBN, and MPy, respectively, at 300 K. At 10 K, however, it is $260 \mu\text{W } \mu\text{m}^{-2}$ for BPT, nearly threefold larger, showing how much harder it is to create picocavities at lower temperature. Similar BPT thresholds are found with 60-nm NPs (fig. S7). Besides this 50-fold variation in critical intensities, the saturation rate P_{op} also depends on molecule type (Fig. 3C, \diamond , and table S2). These observations reinforce that optical heating cannot explain the results, since the tripling of creation rate from ambient $T = 10$ to 300 K does not correspond to the 12,000 K required to exceed U_f .

The formation rate of flares (P_f ; Fig. 3D) is similarly extracted (note S3) and gives very similar I_c with $P_f \propto P_p$, indicating that irradiation plays a similar role in both processes. We note that flare creation rates also depend on the molecule species (although the flare spectral shape does not), emphasizing formation from the same thiol molecule-metal interaction. All these molecules have the same thiol attachment to the lower Au mirror, suggesting that the molecular-dependent effects here arise from the apex of the molecules.

Decay rates

Picocavity decay rates (R_p ; Fig. 3, B and F) are extracted from the distribution of lifetimes (T_p spans 200 ms to 180 s) by performing

maximum log-likelihood estimation (fig. S8, note S4, and table S3). A clear double-exponential distribution is seen, showing that picocavities divide into two types (Fig. 3F), fast and slow (~ 5 -fold longer-lived). The longest characteristic lifetimes of 180 s are observed for MPy, despite it has the lowest intensity threshold. Threefold more fast-decaying than slow-decaying picocavities (Fig. 3F, marker size) is perhaps related to their metastable configurations (molecule-metal transient coordination bonds, as discussed below) (21).

Previously published molecule-atom interactions forming these coordination bonds (32) resolve the effect of their conformation on single-molecule SERS spectra (figs. S9 and S10 and table S5). The carefully calculated DFT Morse potentials (fig. S11) give free energies of binding $U_b^0 \gg k_B T$ (table S6), accounting for their room temperature stability. The slow decay rates are found to be light-activated in a similar way to their creation rates. Decay rates are higher in BPT than in MBN or MPy (again just as for picocavity creation rates), confirming the lower stability of picocavities in BPT as well as the greater difficulty of creating them (Fig. 3E).

Flare decay rates (R_f ; Fig. 3G) are similarly calculated (fig. S8 and table S4), again divided into fast and slow types, the latter being >3 -fold rarer and ~ 8 -fold longer-lived for BPT, similar to picocavities (few flares for MBN or MPy make fast decay rates hard to quantify). For all molecules, the decay rate of flares is ~ 10 -fold higher than that of picocavities, showing that picocavities are more stable.

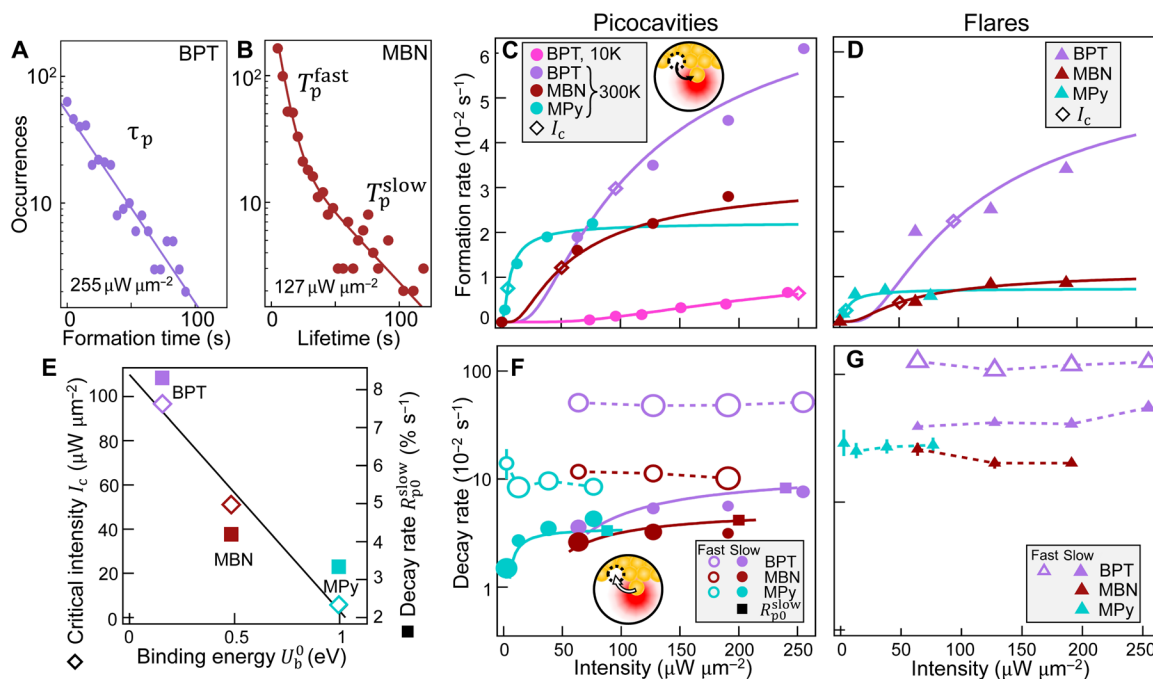


Fig. 3. Formation and decay of picocavities and flares versus laser intensity. (A) Example histogram of formation times and (B) lifetimes of picocavities (log scale). (C) Formation rate of picocavities P_p at room and cryogenic temperatures, solid lines are the fits (see the main text; \diamond marks critical intensities). (D) Formation rate of flares P_f . (E) Critical laser intensity I_c required for picocavity and flare formation [\diamond from (C) and (D)] and saturation decay rate of slow picocavities R_{p0}^{slow} [\blacksquare from (F)] versus molecule-metal binding energy U_b^0 (see note S5, fig. S11, and table S6). (F) Decay rate of picocavities R_p (log scale), split into two classes observed as in (B): fast (open circles, <10 s for BPT and <25 s for MBN and MPy) and slow (filled circles) lifetimes [fit lines from (C)]. (G) Decay rate of flares R_f , with fast (open triangles, <2 s) and slow (filled triangles) lifetimes. In (F) and (G), marker size gives the relative fraction of fast and slow events at each intensity. For BPT, 804,500 spectra are recorded in 1609 time series from 400 NPoMs; for MBN, 42,840 spectra in 357 time series from 119 NPoMs; and for MPy, 42,480 spectra in 236 time series from 59 NPoMs.

DISCUSSION

Picocavities are not seen initially or at the lowest powers (Fig. 1B), which implies that Au⁽⁰⁾ adatoms do not exist on the nanoparticle facets before illumination (which suggests that the strong van der Waals attraction anneals the metal facets completely flat). To understand how light induces Au atom motion, our results point to the influence of molecule type and temperature. The critical intensity for each molecule is found to inversely correlate with their DFT coordination binding energies (Fig. 3E), as well as their decay times. This shows that when a Au adatom can strongly coordinate to the nearby molecule, this aids picocavity creation and retards picocavity decay. The observed exponential waiting time probability $P_p(t) \propto \exp\{-t/\tau_p\}$ for a picocavity to form (Fig. 3A) implies a thermally activated process (rather than deterministically driven by the laser). The picocavity creation rate should thus follow

$$P_p = P_{0p} \exp\{-U_f/k_B T\} \quad (1)$$

As noted, optical heating on its own cannot account for the energies required to abstract Au adatoms, nor is such heating observed in the anti-Stokes ERS, which has been shown to track the metal temperature accurately; if observed temperatures (fig. S12) drive picocavities, this would imply unfeasibly small 5 meV barriers ($\ll U_f$). Such heating also cannot explain why formation is harder at lower initial temperatures or why it saturates at high laser intensities. In the discussion here, we show that optical forces are far too weak to be directly involved and thus explore alternative explanations.

Estimate of optical forces (model 1)

To form adatoms, the Au atom moves $\sim 1.5 \text{ \AA}$ (the atomic radius a), thus requiring typical forces $F_c = \frac{d}{dt} U_f^0 \sim U_f^0/a > 1 \text{ nN}$. Confining the incident intensity $I = \frac{1}{2} c \epsilon_0 |\mathcal{E}_i|^2$ into the gap (speed of light in vacuum c , vacuum permittivity ϵ_0 , and incident light field \mathcal{E}_i) generates optical force $F = \frac{1}{2} \alpha_a \nabla \mathcal{E}^2$ from the optical field gradient around the adatom (Figs. 4, A to C, and fig. S14) (19), with polarizability $\alpha_a = 4\pi\epsilon_0 a^3$ of the adatom sphere. This yields (notes S6 to S8) an optical force in model 1 of $F_0 \sim \eta \mathfrak{N} \mathfrak{E} F^2 a^2 / c$, where $\eta \sim 0.4$ is the coupling efficiency into the resonant plasmonic mode (37), $\mathfrak{E} F \sim 500$ is the local enhancement factor of the optical field in the nanoparticle center at this resonance (fig. S2), and $\mathfrak{N} \sim 4$ accounts for the classical local enhancement (15) of the metal protrusion (fig. S15). For the parameters here, $F_0 \sim 1 \text{ pN}$ per mW illumination, which is four to five orders of magnitude too weak to overcome the adatom extraction force F_c . Considering the resulting potential versus Au adatom position ξ (fig. S20), a further problem with model 1 comes from the optical force that tilts the potential (solid line, Fig. 4D). This reduces the forward barrier for adatom creation $U_f(I)$, but the barrier for its subsequent relaxation $U_b(I)$ is then larger, which implies that adatom decay should not be seen while the light is on. In direct contrast, our observed decay rates match the creation rates (Fig. 3); hence, conventional optical forces cannot be responsible.

Other models considered include hot Au atom excitation (analogous to hot electrons; fig. S23), in which a plasmon gives its entire energy to kick a Au atom over the barrier U_f . However, this should not be temperature or molecule dependent (note S10). We also confirm

that quantum tunneling of the Au atom through this barrier has implausibly low probability.

Light-activated molecule-metal energy barrier reduction (model 2)

For Eq. 1 to match the creation rates observed, the barrier height must reduce with increasing laser intensities. We thus introduce a tentative model to explain how this can occur. We first note that the closest molecule to the adatom influences the locally dressed permittivity in the picocavity field via its effective polarizability α rather than behaving as a uniform dielectric. With the laser on, the adatom acts as an optical dipole [as evidenced in (15)], producing field \mathcal{E}_t at the molecule tip, which polarizes it (Fig. 4C) as $p_t = \alpha_t(\mathcal{E}_t + \mathcal{E}_{im}) = \alpha_t\mathcal{E}_t + \alpha_t\mathcal{N} p/[4\pi\epsilon_0(2z)^3] = \alpha_t\mathcal{E}_t$ where its proximity to the plasmonic metal gives image charges that induce additional field \mathcal{E}_{im} at the molecule (fig. S13). Here, α_t is the tip atom polarizability and z is the separation of the tip atom of the molecule to the classical edge of the adatom. This drastically enhances the effective α (in a quasi-static approximation; see note S8)

$$\frac{\alpha}{\alpha_t} \equiv \zeta \approx \frac{1}{1 - (\kappa/z)^3} \quad (2)$$

where $\kappa = (\alpha_t\mathcal{N}/8)^{1/3}$. In a uniform optical field, typical molecular polarizabilities $\alpha_0 \sim 10 \text{ \AA}^3$ (benzene) give critical separation $\kappa \sim 1.8 \text{ \AA}$, but here, the local polarizability can be much higher since the picocavity field is so nonuniform over a single electronic orbital (Fig. 4C), as estimated by DFT below. In this semiclassical model, for $z < \kappa$, the polarizability becomes infinite, a “polarization catastrophe” thought sufficient to deform/break molecules when close to metals (38). The resulting dipole-dipole (or induced van der Waals) attraction between

the picocavity adatom dipole and the induced molecular dipole enhances the force $F_p \sim F_0 \alpha/\alpha_0$ by $>10^3$. The local polarizability at the molecule tip creates opposite charges at the adatom, inducing an attractive optical force (model 2; Fig. 4E). The attracted molecule comes even closer to the nanoparticle facet, reducing the energy barrier for adatom protrusion. The binding enhances as the molecule approaches, until quantum-wave function repulsion impedes it enough to set the equilibrium molecular separation from the facet.

Above the critical intensity, the barrier becomes low enough for thermal excitation to occur, giving observable picocavities. A simple simulation using this model (fig. S22) indeed suggests that the net energy barrier is controlled by light intensity (Fig. 5A). From Eq. 1, we extract $U_f(I)$, which decreases with power in experiment (Fig. 5D), giving critical intensity at $U_f(I_c) = k_B T$ (dashed line). In this model, both creation and decay of picocavities are similarly light-activated by the barrier reduction (as observed), in contrast to all other models considered. The saturation rate P_{0p} (Fig. 3C) is then controlled by the minimum tip atom-to-adatom separation that is quantum mechanically feasible. Irradiation decreases the barrier height as \mathcal{E}^{-2} , so adatoms are pulled out only in the strongest near-field positions \mathcal{E}_g within the nanogap, dependent on the precise alignment of the closest molecule to prospective adatoms in the facet, as shown in recent experiments (33).

The influence of different molecules at the metal surface can now be related to the tip atom polarizability from local dipolar excitation, which thus decreases barrier height faster for MPy than for BPT. DFT modeling is performed on each molecule (see Materials and Methods), with the tip atom being C for BPT (approaching from out of plane) and N for MBN and MPy. The alignment of the Au adatom is first determined from the minimum energy conformation with relative

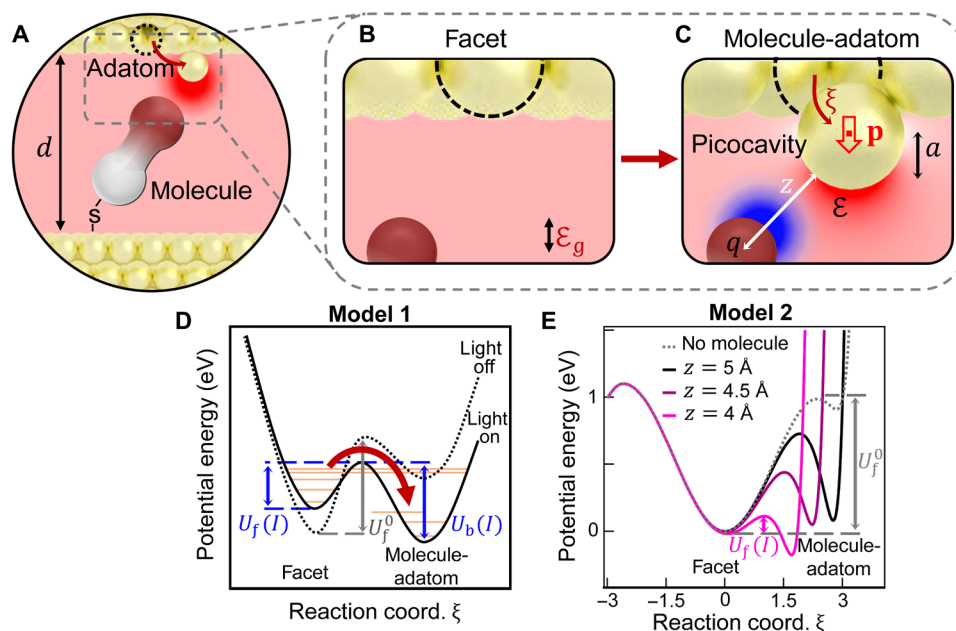


Fig. 4. Proposed mechanism for light-driven changes in molecule-metal binding. (A to C) Scheme of picocavities, with localization of optical field (red) around an adatom, which attracts the molecule tip. Reaction coordinate ξ in (C) is the trajectory distance of the adatom from the initial site in facet of (B), z is the distance from the tip atom (radius a) to the edge of the Au adatom, and \mathbf{p} is the dipole induced by gap optical field \mathcal{E}_g producing picocavity field \mathcal{E} . (D) Model 1: Optical forces in picocavity field gradient tilt the potential when the laser is on (solid) versus off (dashed). U_f^0 is the barrier for adatom formation when the laser is off, and $U_{fb}(I)$ are barriers for adatom formation and decay at laser intensity I . (E) Model 2: Simulated energy for picocavities when molecule tip-adatom separation z decreases by light (solid) versus without molecule (dashed), showing reduced barrier height.

position (figs. S10 and S11 and table S5). The optical excitation is then treated as a dipole of strength p at the Au adatom (Fig. 5, B and E). As the dipole approaches the molecular tip, the induced attractive optical force pulls electrons toward the frontier orbital of the molecular tip atom, changing the charge distribution around it (fig. S17). The resulting induced charge q at the molecular tip atom is mapped versus the relative position of the Au adatom (Fig. 5, C, F, and I). To extract α_t , q is then multiplied by $\cos^2\theta$ (accounting for the orientation of optical field and projection of vector polarizability; note S8) to generate the component of polarizability in the vertical direction (q/p ; Fig. 5G). At theoretical equilibrium separations of $z \sim 2.2$ Å (dashed, similar for all these molecules in DFT; also see fig. S11), the induced charge is ~ 20 -fold larger for MPy than for BPT. This is consistent with the ratio of threshold intensities for picocavity

formation, as I_c is ~ 20 -fold smaller for MPy than for BPT (Fig. 5H). All the light-induced barriers $U_f(I)$ collapse onto a universal curve (fig. S21), well fit by $U_f(I) = U_f^0/(I/I_t + 1)$ (giving Fig. 3C, solid lines), where $I_c = I_t U_f^0/k_B T$.

Optical effects at molecular-metal interfaces are thus drastically different from uniform dielectrics. To treat them fully consistently, we await quantum mechanical solutions for the local optical polarizability at molecules and atomistically modeled metals including treatment of image charges in continuum electromagnetics. However, here we outlined and evidenced the concept of local polarizability at the molecule tip, which controls the energetic landscape (note S9). While the dynamic behavior of metal-molecule nanojunctions previously implicated molecular properties (39, 40), here we demonstrate that it is molecular coordination with adatoms that is important.

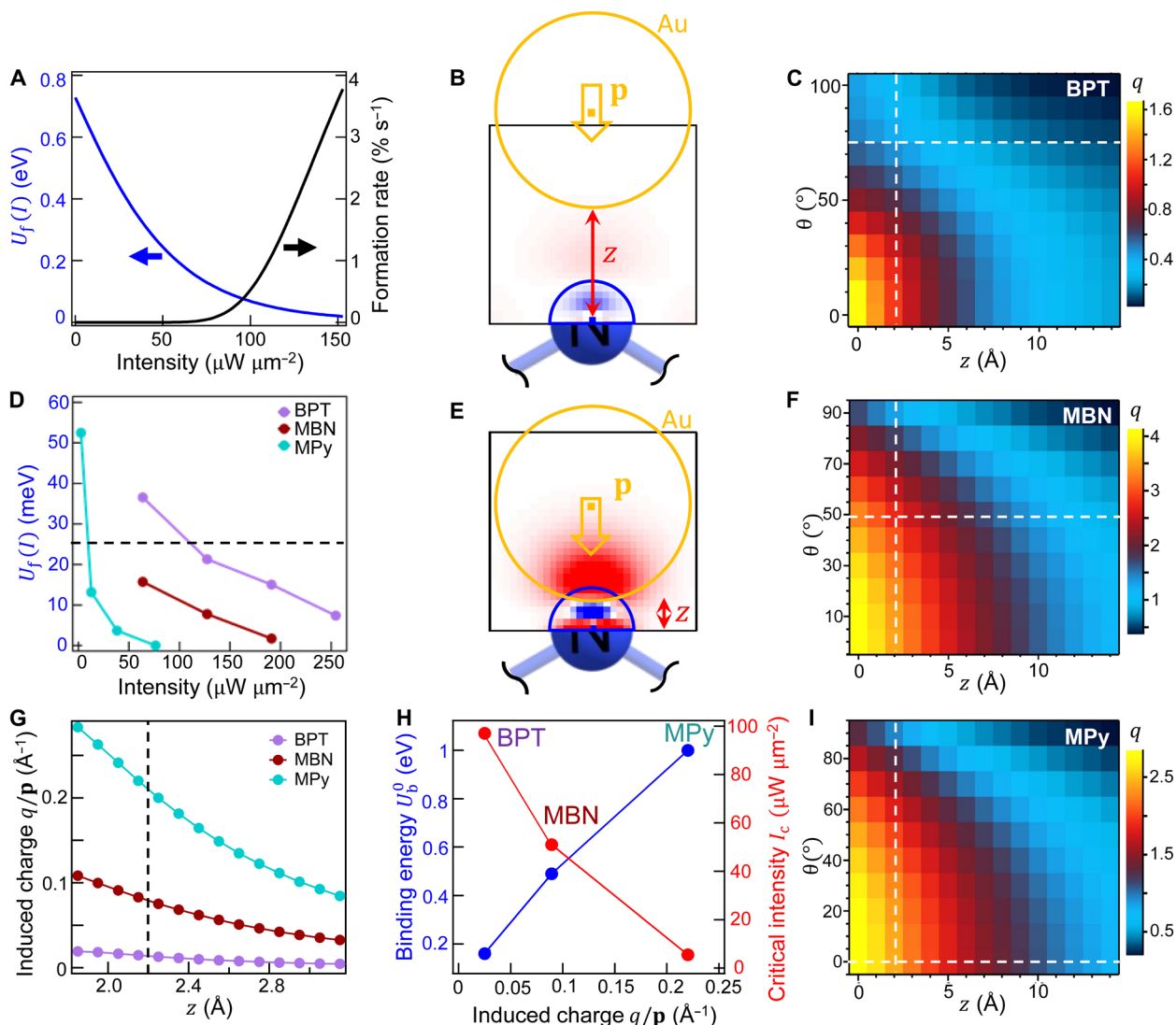


Fig. 5. Light-induced molecule tip atom local polarizability relation to intensity threshold. (A) Simulated dependence of $U_f(I)$ and picocavity formation rate versus laser power in model 2 for BPT. (B and E) DFT-calculated charge q induced on the tip atom (here, N for MPy) when the Au adatom field is treated as an optical dipole of strength p at distance z away. (C, F, and I) Induced charge q , mapped versus adatom position, with z and angle θ on planes perpendicular to the aromatic ring (see fig. S10). Dashed lines show energetically favorable adatom from DFT at $z = 2.2$ Å and $\theta = 75^\circ$, 49° , and 0° for the three molecules. (D) Extracted $U_f(I)$ for different molecules from data, thresholds given by $U_f(I_c) = k_B T$ (dashed). (G) Induced charge q from DFT tracks tip atom polarizability α_t . (H) Molecule-metal binding energy well depth U_b^0 and critical laser intensity I_c required for picocavity and flare formation versus induced charge q at the molecule tip atom.

We also note that our model explains why picocavity decay rates match creation rates, since the light similarly reduces the barrier for adatoms dropping back into the facet. The similar dependence of rates for picocavities and flares also suggests that in flares, many atoms are polarized in parallel by the light.

Our suggested “optical plucking” (model 2) also leaves issues to be resolved. Previous experiments (21, 30) imply that picocavities can form at the bottom gold mirror. The same mechanism is thus likely at work, inducing polarizabilities of the Au-thiol bond but has higher I_c . Although thiols themselves can pull out single gold atoms from the surface, such “staples” (41) are present as Au⁽¹⁾, which is not metallic and does not give picocavity field enhancement. While additional lattice strain might form Au⁽⁰⁾, picocavities are not seen before prolonged exposure to light (Fig. 1B), and the thiol would not be affected by the molecular tip (since S-Au binding is little affected by molecule type). Another issue is the possible relaxation of the remaining atoms surrounding the pit when the adatom is pulled out, leading to metastable configurations. Steric considerations must also be important, since the Au adatom is evidently able to move into the space within the dense SAM.

These experiments demonstrate that light-driven attraction between metal and molecules can promote adatoms and stabilize them for many minutes under ambient conditions. Examining possible mechanisms identifies one that accounts for all observations and is supported by DFT calculations of the local polarizability at the molecule tip closest to the Au. Our findings are not limited to optical irradiation, since applying voltage or injection of electron beams (31) can also induce adatom formation, offering scope for further study. We also observe that adatom formation rates vary on different facets (note S9), opening up complementary future directions to systematically resolve the effects of facet surface structure on picocavity formation, which are of interest in supramolecular chemistry and nanoparticle synthesis.

Our observations apply to many systems, from optically irradiated molecular electronics and photocatalysis to semiconductor-metal optoelectronic devices. In all cases, interactions between a polarizable atom and a metallic atom can create extremely powerful optical forces capable of rearranging the material interface. Detailed observations here come from using precise plasmonic constructs that efficiently and reproducibly trap light as well as providing the sensitivity to quantify what structural changes are occurring. While such plasmonic nanogaps are ideal model systems, similar optical confinement is found in many granular metal photocatalysts or at the sharp asperities of individual nanoparticles, implying that optical restructuring of surfaces is widespread. The model that emerges provides intuition for using light-molecule-metal systems to control single-atom optical switches, photocatalysis, photovoltaics, and sensing. However, this work should also provide strong encouragement to develop new theories capable of combining electromagnetism with quantum mechanics.

MATERIALS AND METHODS

Experimental design

Sample preparation

All chemicals were purchased from Sigma-Aldrich and used as received, unless stated otherwise. Atomically smooth gold substrates were fabricated by template-stripping methods (19, 21). SAMs of BPT, MBN (Santa Cruz Biotechnology), and MPy were formed by immersing the substrates in anhydrous ethanol solution, at concentrations of 1, 2, and 2 mM, respectively, for 16 hours. The substrates were

rinsed with ethanol and dried with nitrogen. Standard AuNPs in citrate buffer were purchased from BBI Solutions (42) with reported morphology (43). AuNPs were deposited by drop-casting either 80 nm AuNP solution onto BPT samples for 60 s, or 60 nm AuNP solution mixed with 40 mM NaNO₃ onto MBN and MPy samples for 20 s. These AuNP sizes are chosen because of their stronger optical response ($\propto D^6$) and high stability. Measuring anti-Stokes-to-Stokes ratios proves that optical heating in our system is below 10 K here so the gold remains at near room temperature ($T < 50^\circ\text{C}$) and no melting occurs (melting point for these NPs, $\sim 1000^\circ\text{C}$), as plasmons do not directly heat the molecules (19) and induced optical heating is negligible (44). The samples were rinsed with deionized water and dried. No SERS signatures of citrate are ever seen from the NPOMs, as expected from the larger binding affinity of thiols that displace them.

SERS measurements

All spectra were recorded on a modified Olympus BX51 microscope coupled to a Raman spectrometer. A Prior Scientific motorized stage was used to move the sample. Dark-field images were recorded using a Lumenera Infinity2 charge-coupled device (CCD) camera. A 632.8-nm single-frequency diode laser was used as the excitation source. Intensities were derived from the laser power on the sample measured using a Thorlabs PM16-121 power meter. For room temperature measurements, the laser was focused on a diffraction-limited spot of diameter $\sim 1\ \mu\text{m}$. Integration times used for BPT, MBN, and MPy were 0.2, 1, and 1 s, respectively. Excitation and collection were performed using a dichroic beamsplitter and an Olympus MPLFLN100XBD NA (numerical aperture) 0.9 objective. Elastically scattered laser light was removed using two Thorlabs NF633-25 notch filters. Scattered light was imaged onto an Andor Newton EMCCD coupled to a HORIBA Triax 320 spectrometer. For low-temperature measurements, the laser was focused on a $\sim 2\text{-}\mu\text{m}$ -diameter spot, and an integration time of 3 s was used. An Oxford Instruments Microstat HiRes cryostat, an Olympus LMPLFLN100XBD NA 0.8 objective, and two Semrock NF03-633E-25 single-notch filters were used. Scattered light was imaged on an Andor Newton EMCCD coupled to an Andor Shamrock 303i spectrometer.

DFT calculations

Molecules were modeled with thiol groups bound to single gold atoms for nanocavity systems (Fig. 2) and to two gold atoms for picocavity systems (fig. S3) to ensure an even number of electrons. Adatoms were modeled as single gold atoms attached to the molecules. Compared with DFT of molecules bound to large gold layers, DFT from binding to one or two gold atoms matches the experimental SERS well (21, 45) at much lower computational cost. Gas-phase geometry optimizations, frequency calculations, and calculations for changes in electron density (Fig. 5) were carried out with no symmetry restrictions. Grimme's D3 dispersion correction with Becke-Johnson damping GD3BJ (46) was used with the B3LYP hybrid functional and the def2TZVP basis set. The ultrafine integration grid was used to enhance the accuracy of calculations. To match the experiment, computational spectra were scaled by a factor of 0.97. The external electric field was modeled in the computations via two +0.1 e and -0.1 e point charges, forming a dipole at grid points near the N atoms (MPy and MBN) or the C atom (BPT) of the molecule. The distance between the point charges is 0.1 Å in all calculations, and the dipole vector points toward the N or C atoms. Changes in electron density were calculated with respect to the unperturbed system. All DFT calculations were carried out with the Gaussian09 Revision E (47).

Statistical analysis

Sample sizes (n) are indicated in the captions of Fig. 3 and fig. S7. Formation rates (P , in second^{-1}) are calculated from the fraction of empty time series where picocavities or flares are not observed (P_{empty}), with details in note S3. Decay rates were extracted by modeling the lifetime (T , in seconds) of each transient event with a biexponential probability density function, with fractions of fast and slow events as detailed in note S4. The statistical results are summarized in tables S1 to S3 and plotted in Fig. 3.

SUPPLEMENTARY MATERIALS

Supplementary material for this article is available at <https://science.org/doi/10.1126/sciadv.abp9285>

REFERENCES AND NOTES

- B. S. Hoener, S. R. Kirchner, T. S. Heiderscheit, S. S. E. Collins, W. S. Chang, S. Link, C. F. Landes, Plasmonic sensing and control of single-nanoparticle electrochemistry. *Chem* **4**, 1560–1585 (2018).
- L. Zhou, D. F. Swearer, C. Zhang, H. Robatjazi, H. Zhao, L. Henderson, L. Dong, P. Christopher, E. A. Carter, P. Nordlander, N. J. Halas, Quantifying hot carrier and thermal contributions in plasmonic photocatalysis. *Science* **362**, 69–72 (2018).
- G. Li, R. Zhu, Y. Yang, Polymer solar cells. *Nat. Photonics* **6**, 153–161 (2012).
- B. Sepúlveda, P. C. Angelomé, L. M. Lechuga, L. M. Liz-Marzán, LSPR-based nanobiosensors. *Nano Today* **4**, 244–251 (2009).
- P. K. Jain, X. Huang, I. H. El-Sayed, M. A. El-Sayed, Noble metals on the nanoscale: Optical and photothermal properties and some applications in imaging, sensing, biology, and medicine. *Acc. Chem. Res.* **41**, 1578–1586 (2008).
- M. Galperin, Photonics and spectroscopy in nanojunctions: A theoretical insight. *Chem. Soc. Rev.* **46**, 4000–4019 (2017).
- N. Xin, J. Guan, C. Zhou, X. Chen, C. Gu, Y. Li, M. A. Ratner, A. Nitzan, J. F. Stoddart, X. Guo, Concepts in the design and engineering of single-molecule electronic devices. *Nat. Rev. Phys.* **1**, 211–230 (2019).
- P. Gehring, J. M. Thijssen, H. S. J. van der Zant, Single-molecule quantum-transport phenomena in break junctions. *Nat. Rev. Phys.* **1**, 381–396 (2019).
- A. R. Rocha, V. M. García-suárez, S. W. Bailey, C. J. Lambert, J. Ferrer, S. Sanvito, Towards molecular spintronics. *Nat. Mater.* **4**, 335–339 (2005).
- L. Bogani, W. Wernsdorfer, Molecular spintronics using single-molecule magnets. *Nat. Mater.* **7**, 179–186 (2008).
- S. Sanvito, Molecular spintronics. *Chem. Soc. Rev.* **40**, 3336–3355 (2011).
- S. Schlücker, Surface-enhanced raman spectroscopy: Concepts and chemical applications. *Angew. Chem. Int. Ed.* **53**, 4756–4795 (2014).
- M. Barbry, P. Koval, F. Marchesin, R. Esteban, A. G. Borisov, J. Aizpurua, D. Sánchez-Portal, Atomistic near-field nanoplasmonics: Reaching atomic-scale resolution in nanooptics. *Nano Lett.* **15**, 3410–3419 (2015).
- S. Trautmann, J. Aizpurua, I. Götz, A. Undisz, J. Dellith, H. Schneidewind, M. Rettenmayr, V. Deckert, A classical description of subnanometer resolution by atomic features in metallic structures. *Nanoscale* **9**, 391–401 (2017).
- M. Urbietta, M. Barbry, Y. Zhang, P. Koval, D. Sánchez-Portal, N. Zabala, J. Aizpurua, Atomic-scale lightning rod effect in plasmonic picocavities: A classical view to a quantum effect. *ACS Nano* **12**, 585–595 (2018).
- R. Zhang, Y. Zhang, Z. C. Dong, S. Jiang, C. Zhang, L. G. Chen, L. Zhang, Y. Liao, J. Aizpurua, Y. Luo, J. L. Yang, J. G. Hou, Chemical mapping of a single molecule by plasmon-enhanced Raman scattering. *Nature* **498**, 82–86 (2013).
- J. Lee, K. T. Crampton, N. Tallarida, V. A. Apkarian, Visualizing vibrational normal modes of a single molecule with atomically confined light. *Nature* **568**, 78–82 (2019).
- M. Richard-Lacroix, V. Deckert, Direct molecular-level near-field plasmon and temperature assessment in a single plasmonic hotspot. *Light Sci. Appl.* **9**, 35 (2020).
- F. Benz, M. K. Schmidt, A. Dreismann, R. Chikkaraddy, Y. Zhang, A. Demetriadou, C. Carnegie, H. Ohadi, B. de Nijs, R. Esteban, J. Aizpurua, J. J. Baumberg, Single-molecule optomechanics in “picocavities”. *Science* **354**, 726–729 (2016).
- H.-H. Shin, G. J. Yeon, H.-K. Choi, S.-M. Park, K. S. Lee, Z. H. Kim, Frequency-domain proof of the existence of atomic-scale SERS hot-spots. *Nano Lett.* **18**, 262–271 (2018).
- C. Carnegie, J. Griffiths, B. de Nijs, C. Readman, R. Chikkaraddy, W. M. Deacon, Y. Zhang, I. Szabó, E. Rosta, J. Aizpurua, J. J. Baumberg, Room-temperature optical picocavities below 1 nm³ accessing single-atom geometries. *J. Phys. Chem. Lett.* **9**, 7146–7151 (2018).
- J. Huang, D.-B. Gryns, J. Griffiths, B. de Nijs, M. Kamp, Q. Lin, J. J. Baumberg, Tracking interfacial single-molecule pH and binding dynamics via vibrational spectroscopy. *Sci. Adv.* **7**, eabp9285 (2021).
- L. Vitos, A. V. Ruban, H. L. Skriver, J. Kollár, The surface energy of metals. *Surf. Sci.* **411**, 186–202 (1998).
- J. Takano, O. Takai, Y. Kogure, M. Doyama, Simulation of atomic-scale surface migration in homoepitaxial growth using embedded-atom method potentials for gold. *Thin Solid Films* **318**, 52–56 (1998).
- Y. Liu, V. Ozolins, Self-assembled monolayers on Au(111): Structure, energetics, and mechanism of reconstruction lifting. *J. Phys. Chem. C* **116**, 4738–4747 (2012).
- D. Thompson, J. Liao, M. Nolan, A. J. Quinn, C. A. Nijhuis, C. O'Dwyer, P. N. Nirmalraj, C. Schönenberger, M. Calame, Formation mechanism of metal–molecule–metal junctions: Molecule-assisted migration on metal defects. *J. Phys. Chem. C* **119**, 19438–19451 (2015).
- T.-S. Lin, Y.-W. Chung, Measurement of the activation energy for surface diffusion in gold by scanning tunneling microscopy. *Surf. Sci.* **207**, 539–546 (1989).
- J. J. Baumberg, J. Aizpurua, M. H. Mikkelsen, D. R. Smith, Extreme nanophotonics from ultrathin metallic gaps. *Nat. Mater.* **18**, 668–678 (2019).
- J. Langer, D. J. de Aberasturi, J. Aizpurua, R. A. Alvarez-Puebla, B. Auguie, J. J. Baumberg, G. C. Bazan, S. E. J. Bell, A. Boisen, A. G. Brolo, J. Choo, D. Cialla-May, V. Deckert, L. Fabris, K. Faulds, F. J. G. de Abajo, R. Goodacre, D. Graham, A. J. Haes, C. L. Haynes, C. Huck, T. Itoh, M. Käll, J. Kneipp, N. A. Kotov, H. Kuang, E. C. Le Ru, H. K. Lee, J.-F. Li, X. Y. Ling, S. A. Maier, T. Mayerhöfer, M. Moskovits, K. Murakoshi, J.-M. Nam, S. Nie, Y. Ozaki, I. Pastoriza-Santos, J. Perez-Juste, J. Popp, A. Pucci, S. Reich, B. Ren, G. C. Schatz, T. Shegai, S. Schlücker, L.-L. Tay, K. G. Thomas, Z.-Q. Tian, R. P. Van Duyne, T. Vo-Dinh, Y. Wang, K. A. Willets, C. Xu, H. Xu, Y. Xu, Y. S. Yamamoto, B. Zhao, L. M. Liz-Marzán, Present and future of surface-enhanced raman scattering. *ACS Nano* **14**, 28–117 (2020).
- C. Carnegie, M. Urbietta, R. Chikkaraddy, B. de Nijs, J. Griffiths, W. M. Deacon, M. Kamp, N. Zabala, J. Aizpurua, J. J. Baumberg, Flickering nanometre-scale disorder in a crystal lattice tracked by plasmonic flare light emission. *Nat. Commun.* **11**, 682 (2020).
- F. Benz, B. de Nijs, C. Tserkezis, R. Chikkaraddy, D. O. Sagle, L. Pukenas, S. D. Evans, J. Aizpurua, J. J. Baumberg, Generalized circuit model for coupled plasmonic systems. *Opt. Express* **23**, 33255–33269 (2015).
- J. Griffiths, T. Földes, B. de Nijs, R. Chikkaraddy, D. Wright, W. M. Deacon, D. Berta, C. Readman, D. B. Gryns, E. Rosta, J. J. Baumberg, Resolving sub-angstrom ambient motion through reconstruction from vibrational spectra. *Nat. Commun.* **12**, 6759 (2021).
- J. Griffiths, B. de Nijs, R. Chikkaraddy, J. J. Baumberg, Locating single-atom optical picocavities using wavelength-multiplexed raman scattering. *ACS Photonics* **8**, 2868–2875 (2021).
- Y.-Y. Cai, E. Sung, R. Zhang, L. J. Tauzin, J. G. Liu, B. Ostovar, Y. Zhang, W.-S. Chang, P. Nordlander, S. Link, Anti-stokes emission from hot carriers in gold nanorods. *Nano Lett.* **19**, 1067–1073 (2019).
- B. de Nijs, R. W. Bowman, L. O. Herrmann, F. Benz, S. J. Barrow, J. Mertens, D. O. Sagle, R. Chikkaraddy, A. Eiden, A. Ferrari, O. A. Scherman, J. J. Baumberg, Unfolding the contents of sub-nm plasmonic gaps using normalising plasmon resonance spectroscopy. *Faraday Discuss.* **178**, 185–193 (2015).
- J. N. Sweet, The spectral similarity scale and its application to the classification of hyperspectral remote sensing data, in *IEEE Workshop on Advances in Techniques for Analysis of Remotely Sensed Data* (IEEE, 2003), pp. 92–99.
- N. Kongsuwan, A. Demetriadou, M. Horton, R. Chikkaraddy, J. J. Baumberg, O. Hess, Plasmonic nanocavity modes: From near-field to far-field radiation. *ACS Photonics* **7**, 463–471 (2020).
- C. M. Teodorescu, Image molecular dipoles in surface enhanced Raman scattering. *Phys. Chem. Chem. Phys.* **17**, 21302–21314 (2015).
- W. Du, T. Wang, H.-S. Chu, L. Wu, R. Liu, S. Sun, W. K. Phua, L. Wang, N. Tomczak, C. A. Nijhuis, On-chip molecular electronic plasmon sources based on self-assembled monolayer tunnel junctions. *Nat. Photonics* **10**, 274–280 (2016).
- T. Wang, W. Du, N. Tomczak, L. Wang, C. A. Nijhuis, In operando characterization and control over intermittent light emission from molecular tunnel junctions via molecular backbone rigidity. *Adv. Sci.* **6**, 1900390 (2019).
- H. Häkkinen, The gold–sulfur interface at the nanoscale. *Nat. Chem.* **4**, 443–455 (2012).
- BBI Solutions, *Diagnostic Gold Colloid*; www.bbisolutions.com/en/reagents/gold-colloid.
- F. Benz, R. Chikkaraddy, A. Salmon, H. Ohadi, B. de Nijs, J. Mertens, C. Carnegie, R. W. Bowman, J. J. Baumberg, SERS of individual nanoparticles on a mirror: Size does matter, but so does shape. *J. Phys. Chem. Lett.* **7**, 2264–2269 (2016).
- G. Baffou, R. Quidant, F. J. García de Abajo, Nanoscale control of optical heating in complex plasmonic systems. *ACS Nano* **4**, 709–716 (2010).
- D. Wright, Q. Lin, D. Berta, T. Földes, A. Wagner, J. Griffiths, C. Readman, E. Rosta, E. Reisner, J. J. Baumberg, Mechanistic study of an immobilized molecular electrocatalyst by in situ gap-plasmon-assisted spectro-electrochemistry. *Nat. Catal.* **4**, 157–163 (2021).
- A. Allouche, Software news and updates Gabedit—A graphical user interface for computational chemistry softwares. *J. Comput. Chem.* **32**, 174–182 (2012).
- M. J. Frisch, G. W. Trucks, H. B. Schlegel, G. E. Scuseria, M. A. Robb, J. R. Cheeseman, G. Scalmani, V. Barone, B. Mennucci, G. A. Petersson, H. Nakatsuji, M. Caricato, X. Li,

- H. P. Hratchian, A. F. Izmaylov, J. Bloino, G. Zheng, J. L. Sonnenberg, M. Hada, M. Ehara, K. Toyota, R. Fukuda, J. Hasegawa, M. Ishida, T. Nakajima, Y. Honda, O. Kitao, H. Nakai, T. Vreven, J. A. Montgomery, J. E. Peralta, F. Ogliaro, M. Bearpark, J. J. Heyd, E. Brothers, K. N. Kudin, V. N. Staroverov, R. Kobayashi, J. Normand, K. Raghavachari, A. Rendell, J. C. Burant, S. S. Iyengar, J. Tomasi, M. Cossi, N. Rega, J. M. Millam, M. Klene, J. E. Knox, J. B. Cross, V. Bakken, C. Adamo, J. Jaramillo, R. Gomperts, R. E. Stratmann, O. Yazyev, A. J. Austin, R. Cammi, C. Pomelli, J. W. Ochterski, R. L. Martin, K. Morokuma, V. G. Zakrzewski, G. A. Voth, P. Salvador, J. J. Dannenberg, S. Dapprich, A. D. Daniels, Ö. Farkas, J. B. Foresman, J. V. Ortiz, J. Cioslowski, D. J. Fox, Gaussian 09 Revision E (2009).
48. T. Giannakopoulos, PyAudioAnalysis: An open-source python library for audio signal analysis. *PLOS ONE* **10**, e0144610 (2015).
49. A. Moroz, Depolarization field of spheroidal particles. *J. Opt. Soc. Am. B* **26**, 517 (2009).
50. E. M. Purcell, D. J. Morin, *Electricity and Magnetism* (Cambridge Univ. Press, ed. 3, 2013).
51. F. D. Nunes, T. C. Vasconcelos, M. Bezerra, J. Weiner, Electromagnetic energy density in dispersive and dissipative media. *J. Opt. Soc. Am. B* **28**, 1544–1552 (2011).
52. A. Ashkin, Optical trapping and manipulation of neutral particles using lasers. *Proc. Natl. Acad. Sci.* **94**, 4853–4860 (1997).
53. D.-B. Gryns, B. de Nijs, A. R. Salmon, J. Huang, W. Wang, W.-H. Chen, O. A. Scherman, J. J. Baumberg, Citrate coordination and bridging of gold nanoparticles: The role of gold adatoms in AuNP aging. *ACS Nano* **14**, 8689–8696 (2020).
54. M. Giesen, Step and island dynamics at solid/vacuum and solid/liquid interfaces. *Prog. Surf. Sci.* **68**, 1–154 (2001).
55. N. V. Smith, C. T. Chen, M. Weinert, Distance of the image plane from metal surfaces. *Phys. Rev. B* **40**, 7565–7573 (1989).
56. A. Xomalis, R. Chikkaraddy, E. Oksenberg, I. Shlesinger, J. Huang, E. C. Garnett, A. F. Koenderink, J. J. Baumberg, Controlling optically driven atomic migration using crystal-facet control in plasmonic nanocavities. *ACS Nano* **14**, 10562–10568 (2020).
57. M. J. Horton, O. S. Ojambati, R. Chikkaraddy, W. M. Deacon, N. Kongsuwan, A. Demetriadou, O. Hess, J. J. Baumberg, Nanoscopy through a plasmonic nanolens. *Proc. Natl. Acad. Sci.* **117**, 2275–2281 (2020).
58. M. Grzelczak, J. Pérez-Juste, P. Mulvaney, L. M. Liz-Marzán, Shape control in gold nanoparticle synthesis. *Chem. Soc. Rev.* **37**, 1783–1791 (2008).
59. O. S. Ojambati, R. Chikkaraddy, W. M. Deacon, J. Huang, D. Wright, J. J. Baumberg, Efficient generation of two-photon excited phosphorescence from molecules in plasmonic nanocavities. *Nano Lett.* **20**, 4653–4658 (2020).
60. C. Latouche, Y.-R. Lin, Y. Tobon, E. Furet, J.-Y. Saillard, C.-W. Liu, A. Boucekkine, Au–Au chemical bonding induced by UV irradiation of dinuclear gold(I) complexes: A computational study with experimental evidence. *Phys. Chem. Chem. Phys.* **16**, 25840–25845 (2014).
61. H. Kuramochi, S. Takeuchi, M. Iwamura, K. Nozaki, T. Tahara, Tracking photoinduced Au–Au bond formation through transient terahertz vibrations observed by femtosecond time-domain raman spectroscopy. *J. Am. Chem. Soc.* **141**, 19296–19303 (2019).

Acknowledgments: We appreciate many useful conversations with A. Demetriadou, J. Aizpurua, H. Sadeghi, and D. Thomson. **Funding:** We acknowledge funding from the EPSRC (EP/L027151/1, EP/R013012/1, and Cambridge NanoDTC EP/L015978/1 to D.W.) and the ERC (project no. 883703 PICOFORCE, 861950 POSEIDON, and 757850 BioNet). B.d.N. acknowledges support from the Royal Society (URF\R1\211162). We acknowledge the U.K. Materials and Molecular Modelling Hub for computational resources, which is partially funded by EPSRC (EP/P020194/1), and the Rosalind research computing facility at King's College London (<https://rosalind.kcl.ac.uk>). **Author contributions:** Q.L., S.H., and J.J.B. conceived the research and developed the experiments. T.F. and E.R. carried out DFT calculations to derive the polarizability for the underlying mechanism. SERS experiments were performed by S.H., Q.L., and J.H. aided by B.d.N. and E.E. Q.L. and T.F. obtained DFT calculations to match the SERS spectra. J.H. and D.W. provided input on interpretation of the results. J.G. helped with the formation and decay rate analysis. Q.L., S.H., T.F., E.R., and J.J.B. analyzed the data and wrote the manuscript with contributions from all authors. **Competing interests:** The authors declare that they have no competing interests. **Data and materials availability:** All data needed to evaluate the conclusions in the paper are present in the paper and/or the Supplementary Materials. Data were archived at DOI: 10.17863/CAM.83932.

Submitted 7 March 2022

Accepted 6 May 2022

Published 24 June 2022

10.1126/sciadv.abp9285

Optical suppression of energy barriers in single molecule-metal binding

Qianqi LinShu HuTamás FöldesJunyang HuangDemelza WrightJack GriffithsEoin ElliottBart de NijsEdina RostaJeremy J. Baumberg

Sci. Adv., 8 (25), eabp9285. • DOI: 10.1126/sciadv.abp9285

View the article online

<https://www.science.org/doi/10.1126/sciadv.abp9285>

Permissions

<https://www.science.org/help/reprints-and-permissions>

Use of this article is subject to the [Terms of service](#)

Science Advances (ISSN) is published by the American Association for the Advancement of Science. 1200 New York Avenue NW, Washington, DC 20005. The title *Science Advances* is a registered trademark of AAAS.

Copyright © 2022 The Authors, some rights reserved; exclusive licensee American Association for the Advancement of Science. No claim to original U.S. Government Works. Distributed under a Creative Commons Attribution License 4.0 (CC BY).